Final assessment of radioactive impurities in the JUNO detector

Thomas Adam[37] Fengpeng An (安丰鹏)[14] Costas Andreopoulos[64] Giuseppe Andronico[47] Nikolay Anfimov[59] Vito Antonelli[49] Tatiana Antoshkina[59] João Pedro Athayde Marcondes de André[37] Didier Auguste[35] Nikita Balashov[59] Andrea Barresi[50] Davide Basilico[49] Eric Baussan[37] Marco Beretta[49] Antonio Bergnoli[52] Nikita Bessonov[59] Daniel Bick[41] Lukas Bieger[46] Svetlana Biktemerova[59] Thilo Birkenfeld[40] Simon Blyth[3] Manuel Böhles[43] Anastasia Bolshakova[59] Mathieu Bongrand[39] Matteo Borghesi[50] Dominique Breton[35] Augusto Brigatti[49] Riccardo Brugnera[53] Riccardo Bruno[47] Antonio Budano[56] Jose Busto[38] Marcel Büchner[43] Anatael Cabrera[35] Barbara Caccianiga[49] Hao Cai (蔡浩)[25] Xiao Cai (蔡啸)[3] Yi-zhou Cai (蔡以周)[19] Stéphane Callier[36] Antonio Cammi[51] Guofu Cao (曹国富)[3] Jun Cao (曹俊)[3,4] Yaoqi Cao (曹尧齐)[65,64] Rossella Caruso[47] Cédric Cerna[36] Vanessa Cerrone[53] Jinfan Chang (常劲帆)[3] Yun Chang (张昀)[30] Tim Charisse[45,43] Chao Chen (陈超)[3] Haotian Chen (陈浩天)[3] Jiahui Chen[14] Jian Chen (陈建)[14] Jing Chen (陈静)[14] Junyou Chen (陈俊有)[20] Pingping Chen (陈平平)[11] Shaomin Chen (陈少敏)[6] Shiqiang Chen (陈士强)[19] Yixue Chen[5] Yu Chen (陈羽)[14] Ze Chen (陈泽)[45,43] Zhangming Chen (陈张铭)[21] Zhiyuan Chen (陈志源)[3,12] Zhongchang Chen[23] Jie Cheng (程捷)[5] Yaping Cheng (程雅苹)[2] Yu Chin Cheng[32] Alexander Chepurnov[59] Alexey Chetverikov[59] Davide Chiesa[50] Ziliang Chu[3] Artem Chukanov[59] Gérard Claverie[36] Catia Clementi[54] Barbara Clerbaux[1] Claudio Coletta[50] Marta Colomer Molla[1] Selma Conforti Di Lorenzo[36] Chenyang Cui (崔晨阳)[3] Lorenzo Vincenzo D'Auria[53] Christophe De La Taille[36] Luis Delgadillo Franco[3,12] Ziyan Deng (邓子艳)[3] Xiaoyu Ding[18] Xuefeng Ding (丁雪峰)[3] Yayun Ding (丁雅韵)[3] Sergey Dmitrievsky[59] Dmitry Dolzhikov[59] Chuanshi Dong (董川石)[3] Haojie Dong (董灏杰)[3] Jianmeng Dong (董建蒙)[6] Marcos Dracos[37] Frédéric Druillole[36] Ran Du (杜然)[3] Shuxian Du[28] Katherine Dugas[66] Stefano Dusini[52] Hongyue Duyang (杜杨洪岳)[18] Jessica Eck[46] Andrea Fabbri[56] Ulrike Fahrendholz[44] Gaofeng Fan (樊高峰)[19] Lei Fan (樊磊)[3] Liangqianjin Fan (范良前进)[3] Jian Fang (方建)[3] Wenxing Fang (方文兴)[3] Dmitry Fedoseev[59] Qichun Feng (冯启春)[15] Shaoting Feng[23] Giovanni Ferrante[50] Daniela Fetzer[43] Marcellin Fotzé[37] Amélie Fournier[36] Aaron Freegard[21] Ying Fu (付颖)[3,12] Feng Gao[1] Alberto Garfagnini[53] Arsenii Gavrikov[22] Diwash Ghimire[21] Marco Giammarchi[49] Nunzio Giudice[47] Maxim Gonchar[59] Guanda Gong (宫冠达)[3,12] Guanghua Gong (龚光华)[6] Yuri Gornushkin[59] Marco Grassi[53] Maxim Gromov[59] Vasily Gromov[59] Minhao Gu (顾旻皓)[3] Xiaofei Gu (谷肖飞)[28] Yu Gu (古宇)[13] Mengyun Guan (关梦云)[3] Yuduo Guan (管宇铎)[3] Nunzio Guardone[47] Rosa Maria Guizzetti[53] Cong Guo (郭聪)[3] Wanlei Guo (郭万磊)[3] Caren Hagner[41] Hechong Han[3] Yang Han (韩阳)[35] Chuanhui Hao (郝传晖)[6] Miao He (何苗)[3] Wei He (何伟)[3] Xinhai He (贺新海)[3] Ziou He (赫子欧)[65,64] Patrick Hellmuth[36] Yuekun Heng (衡月昆)[3] YuenKeung Hor (贺远强)[14] Shaojing Hou (侯少静)[3] Fatima Houria[49] Yee Hsiung (熊怡)[32] Bei-Zhen Hu (胡贝桢)[31] Jun Hu (胡俊)[3] Tao Hu (胡涛)[3] Lian-Chen Huang (黄濂宸)[57] Guihong Huang (黄桂鸿)[17] Jinhao Huang[3] Junlin Huang (黄俊霖)[13] Junting Huang (黄俊挺)[21] Kaixuan Huang (黄凯旋)[14] Shengheng Huang (黄生恒)[17] Tao Huang (黄涛)[14] Xin Huang[3] Xingtao Huang (黄性涛)[18] Yongbo Huang (黄永波)[20] Jiaqi Hui (惠加琪)[21] Lei Huo[15] Cédric Huss[36] Ammad Ul Islam[56] Adrienne Jacobi[66] Arshak Jafar[43] Xiangpan Ji (季向盼)[24] Xiaolu Ji (季筱璐)[3] Junji Jia (贾俊基)[25] Cailian Jiang (江彩莲)[19] Chengbo Jiang (姜承博)[5] Guangzheng Jiang[9] Junjie Jiang (江俊洁)[21] Xiaoshan Jiang (江晓山)[3] Xiaozhao Jiang[3] Yijian Jiang (姜轶剑)[5] Yixuan Jiang (蒋奕萱)[3] Xiaoping Jing (荆小平)[3] Cécile Jollet[36] Liam Jones[64,65] Amina Khatun[1,60] Khanchai Khosonthongkee[63] Denis Korablev[59] Alexey Krasnoperov[59] Sindhujha Kumaran[66] Chun-Hao Kuo (郭君豪)[57] Nikolay Kutovskiy[59] Loïc Labit[37] Tobias Lachenmaier[46] Haojing Lai (赖浩菁)[21] Cecilia Landini[49] Lorenzo Lastrucci[53] Sébastien Leblanc[36] Matthieu Lecocq[36] Ruiting Lei (雷瑞庭)[11]

Received 21 July 2026; Accepted 14 October 2026

©2026 Chinese Physical Society and the Institute of High Energy Physics of the Chinese Academy of Sciences and the Institute of Modern Physics of the Chinese Academy of Sciences and IOP Publishing Ltd. All rights, including for text and data mining, AI training, and similar technologies, are reserved.

CPC Accepted

Rupert Leitner[33] Petr Lenskii[59] Demin Li (李德民)[28] Fei Li (李飞)[3] Gaosong Li (李高嵩)[3] Jiajun Li (李佳俊)[14] Meiou Li (李美鸥)[17] Min Li (李民)[37] Nan Li[8] Ruhui Li (李茹慧)[3] Rui Li (李瑞)[21] Shanfeng Li (黎山峰)[11] Shuo Li (李硕)[19] Teng Li (李腾)[18] Weidong Li (李卫东)[3] Xiaonan Li (李小男)[12] Yichen Li (李依宸)[3] Yifan Li[3] Yingke Li (李应可)[20] Yufeng Li (李玉峰)[3] Zhaohan Li[3] Zhibing Li (李志兵)[14] Zi-Ming Li[28] An-An Liang (梁安安)[29] Jiajun Liao (廖佳军)[14] Minghua Liao (廖明华)[14] Yilin Liao (廖依林)[21] Ayut Limphirat[63] Bo-Chun Lin[29] Guey-Lin Lin (林貴林)[29] Shengxin Lin (林盛鑫)[11] Tao Lin (林韬)[3] Xingyi Lin (林兴毅)[20] Jiajie Ling (凌家杰)[14] Xin Ling (凌鑫)[3] Ivano Lippi[52] Caimei Liu[3] Fang Liu (刘芳)[5] Haidong Liu[28] Hongbang Liu (刘宏邦)[20] Hongjuan Liu (刘红娟)[16] Jianglai Liu (刘江来)[21,22] Jiaxi Liu[3] Jinchang Liu (刘金昌)[3] Kainan Liu (刘凯楠)[17] Min Liu (刘敏)[16] Qian Liu (刘倩)[7] Shenghui Liu (刘生辉)[3] Shulin Liu (刘术林)[3] Ximing Liu (刘希明)[24] Xuewei Liu (刘学伟)[6] Yankai Liu (刘颜恺)[26] Yiqi Liu (刘逸祺)[6] Zhipeng Liu (刘志鹏)[3] Zhuo Liu (刘卓)[3] Lorenzo Loi[51] Paolo Lombardi[49] Kai Loo[34] Haoqi Lu (路浩奇)[3] Junguang Lu (吕军光)[3] Meishu Lu (卢玫澍)[44] Shuxiang Lu (路书祥)[28] Xianguo Lu (卢显国)[65] Bayarto Lubsandorzhiev[59] Sultim Lubsandorzhiev[59] Livia Ludhova[45,43] Arslan Lukanov[59] Fengjiao Luo (罗凤娇)[16] Guang Luo (罗光)[14] Jianyi Luo (罗坚义)[17] Shu Luo (罗舒)[27] Wuming Luo (罗武鸣)[3] Xiaojie Luo (罗晓杰)[3] Bangzheng Ma (马帮争)[18] Bing Ma (马冰)[28] Qiumei Ma[3] Si Ma (马斯)[3] Wing Yan Ma (马咏恩)[18] Xiaoyan Ma (马骁妍)[3] Xubo Ma (马续波)[5] Jihane Maalmi[35] Jingyu Mai (麦景宇)[14] Marco Malabarba[45,43] Yury Malyshkin[45] Roberto Carlos Mandujano[66] Fabio Mantovani[48] Stefano M. Mari[56] Agnese Martini[55] Johann Martyn[43] Matthias Mayer[44] Yue Meng (孟月)[21] Anselmo Meregaglia[36] Lino Miramonti[49] Michele Montuschi[48] Cristobal Morales Reveco[45,40,43] Iwan Morton-Blake[22] Xiangyi Mu (牟向翊)[3] Lakshmi Murgod[3] Massimiliano Nastasi[50] Dmitry V. Naumov[59] Elena Naumova[59] Igor Nemchenok[59] Elisabeth Neuerburg[40] Feipeng Ning (宁飞鹏)[3] Zhe Ning (宁哲)[3] Yujie Niu (牛玉杰)[3] Lothar Oberauer[44] Juan Pedro Ochoa-Ricoux[66] Alexander Olshevskiy[59] Domizia Orestano[56] Fausto Ortica[54] Rainer Othegraven[43] Yifei Pan (潘一飞)[14] Alessandro Paoloni[55] George Parker[43] Yatian Pei (裴亚田)[3] Luca Pelicci[49,40] Anguo Peng (彭安国)[16] Yu Peng[3] Zhaoyuan Peng[3] Elisa Percalli[49] Willy Perrin[37] Frédéric Perrot[36] Fabrizio Petrucci[56] Oliver Pilarczyk[43] Pascal Poussot[37] Ezio Previtali[50] Fazhi Qi (齐法制)[3] Ming Qi (祁鸣)[19] Sen Qian (钱森)[3] Xiaohui Qian (钱小辉)[3] Zhonghua Qin (秦中华)[3] Shoukang Qiu (丘寿康)[16] Manhao Qu[28] Zhenning Qu (曲振宁)[3] Gioacchino Ranucci[49] Thomas Raymond[37] Alessandra Re[49] Abdel Rebii[36] Bin Ren (任斌)[11] Yuhan Ren (任雨涵)[3] Barbara Ricci[48] Mariam Rifai[45,40,43] Mathieu Roche[36] Narongkiat Rodphai[3] Aldo Romani[54] Bedřich Roskovec[33] Félix Rosso[1] Peter Rudakov[59] Arseniy Rybnikov[59] Andrey Sadovsky[59] Sahar Safari[43] Ujwal Santhosh[45,43] Utane Sawangwit[62] Michaela Schever[42,40] Cédric Schwab[37] Konstantin Schweizer[44] Alexandr Selyunin[59] Andrea Serafini[52] Mariangela Settimo[39] Junyu Shao (邵俊禹)[3] Anurag Sharma[46] Vladislav Sharov[59] Hangyu Shi (石航宇)[14] Jingyan Shi (石京燕)[3] Yuan Shi (石源)[3] Hexi Shi (施赫胁)[56] Dmitrii Shpotya[59] Yike Shu (舒以科)[3] Yuhan Shu (舒宇涵)[3] She Shuai (佘帅)[28] Vitaly Shutov[59] Randhir Singh[3,12] Apeksha Singhal[45] Chiara Sirignano[53] Jaruchit Siripak[63] Monica Sisti[50] Mikhail Smirnov[41] Oleg Smirnov[59] Sergey Sokolov[59] Julanan Songwadhana[63] Albert Sotnikov[59] Achim Stahl[40] Luca Stanco[52] Elia Stanescu Farilla[56] Hans Steiger[44,43] Jochen Steinmann[40] Tobias Sterr[46] Matthias Raphael Stock[44] Virginia Strati[48] Mikhail Strizh[59] Aoqi Su[28] Jun Su (苏军)[14] Guangbao Sun (孙光豹)[25] Mingxia Sun (孙明霞)[3] Xilei Sun (孙希磊)[3] Yongzhao Sun (孙永昭)[3] Zhengyang Sun[22] Narumon Suwonjandee[61] Fedor Šimkovic[60] Akira Takenaka[14] Xiaohan Tan (谭晓晗)[18] Haozhong Tang (唐浩忠)[3] Jian Tang (唐健)[14] Jingzhe Tang[20] Quan Tang (唐泉)[16] Xiao Tang (唐晓)[3] Vidhya Thara Hariharan[41] Yuxin Tian[22] Igor Tkachev[59] Tomas Tmej[33] Marco Danilo Claudio Torri[49] Andrea Triossi[53] Wladyslaw Trzaska[34] Andrei Tsaregorodtsev[38] Yu-Chen Tung (董育宸)[57] Cristina Tuve[47] Carlo Venettacci[56] Giuseppe Verde[47] Benoit Viaud[39] Vit Vorobel[33] Lucia Votano[55] Jiawei Wan (万家威)[19] Caishen Wang (王彩申)[11] Chung-Hsiang Wang (王正祥)[30] En Wang (王恩)[28] Hanwen Wang[3] Jiabin Wang (王家斌)[18] Jun Wang (王俊)[14] Ke Wang[23] Li Wang[28,3] Meng Wang (王孟)[16] Meng Wang (王萌)[18] Mingyuan Wang (王明远)[3] Ruiguang Wang (王瑞光)[3] Sibo Wang (王思博)[3] Tianhong Wang (王天鸿)[15] Wei Wang (王为)[14] Wenshuai Wang (王文帅)[3] Wenyuan Wang (王文源)[18] Xi Wang[8] Yangfu Wang (王仰夫)[3]

CPC Accepted

Yaoguang Wang (王耀光)[18] Yi Wang (王毅)[3] Yifang Wang (王贻芳)[3] Yuyi Wang (王宇逸)[6] Zhe Wang (王喆)[6]
Zheng Wang (王铮)[3] Zhimin Wang (王志民)[3] Apimook Watcharangkool[62] Junya Wei (魏俊雅)[18]
Jushang Wei (魏居尚)[18] Wei Wei (魏微)[3] Wei Wei (魏巍)[18] Yuehuan Wei (魏月环)[14] Zhengbao Wei[20]
Liangjian Wen (温良剑)[3] Jun Weng (翁俊)[6] Rosmarie Wirth[45] Bi Wu (吴比)[14] Chengxin Wu (吴城鑫)[14]
Qun Wu (吴群)[18] Yinhui Wu (吴寅慧)[3] Zhaoxiang Wu (吴肇祥)[3] Zhi Wu (吴智)[3] Michael Wurm[43]
Jacques Wurtz[37] Dongmei Xia[10] Shishen Xian (咸世莘)[22] Ziqian Xiang (向子谦)[21] Fei Xiao (肖菲)[3] Pengfei Xiao[3]
Tianying Xiao (肖天颖)[20] Xiang Xiao (肖翔)[14] Wei-Jun Xie[29] Yuguang Xie (谢宇广)[3] Zhizhong Xing (邢志忠)[3]
Benda Xu (续本达)[6] Cheng Xu (徐程)[16] Chuang Xu (徐闯)[6] Donglian Xu (徐东莲)[22,21] Fanrong Xu (徐繁荣)[13]
Jiayang Xu (徐嘉洋)[3] Jilei Xu (徐吉磊)[3] Jinghuan Xu (徐靖桓)[20] Meihang Xu (徐美杭)[3] Shiwen Xu (许释文)[3]
Xunjie Xu (许勋杰)[3] Dongyang Xue (薛东阳)[6] Jingqin Xue (薛景秦)[3] Baojun Yan (闫保军)[3] Qiyu Yan (严启宇)[7,65]
Taylor Yan[63] Xiongbo Yan (严雄波)[3] Changgen Yang (杨长根)[3] Chengfeng Yang (杨成峰)[14] Dikun Yang[23]
Fengfan Yang (杨冯帆)[3] Jie Yang (杨洁)[28] Kaiwei Yang (杨开为)[3,7] Lei Yang (杨雷)[11] Pengfei Yang (杨鹏飞)[14]
Xiaoyu Yang (杨晓宇)[3] Xuhui Yang (杨旭晖)[3] Yifan Yang[1] Zekun Yang (杨泽坤)[64] Haifeng Yao (姚海峰)[3]
Jiaxuan Ye[3] Mei Ye (叶梅)[3] Ziping Ye[22] Frédéric Yermia[39] Jilong Yin (尹纪龙)[3] Weiqing Yin[3]
Xiaohao Yin (尹小豪)[14] Zhengyun You (尤郑昀)[14] Boxiang Yu (俞伯祥)[3] Chiye Yu (余炽业)[11]
Chunxu Yu (喻纯旭)[24] Hongzhao Yu (余泓钊)[3,12] Peidong Yu (于佩东)[3] Simi Yu (禹思蜜)[17] Zeyuan Yu (于泽源)[3]
Cenxi Yuan (袁岑溪)[14] Chengzhuo Yuan (袁成卓)[3] Noman Zafar[58] Vitalii Zavadskyi[59] Fanrui Zeng (曾凡蕊)[18]
Shan Zeng (曾珊)[3] Tingxuan Zeng (曾婷轩)[3] Liang Zhan (占亮)[3] Bin Zhang (张斌)[28] Feiyang Zhang[21]
Han Zhang (张涵)[3] Hangchang Zhang (张航畅)[3] Haosen Zhang[3] Honghao Zhang (张宏浩)[14]
Jiawen Zhang (张家文)[3] Jie Zhang (张杰)[3] Jingbo Zhang (张景波)[15] Junwei Zhang[20] Lei Zhang (张雷)[19]
Ping Zhang (张平)[21] Qingmin Zhang (张清民)[26] Rongping Zhang (张荣凭)[3] Shiqi Zhang (张石其)[14]
Shuihan Zhang (张水涵)[3] Tao Zhang (张涛)[21] Xiaomei Zhang (张晓梅)[3] Xu Zhang (张叙)[3]
Xuantong Zhang (张玄同)[3] Yibing Zhang (张依兵)[3,12] Yinhong Zhang (张银鸿)[3] Yiyu Zhang (张易于)[3]
Yongpeng Zhang (张永鹏)[3] Yuanyuan Zhang[22] Yue Zhang (张越)[18] Yumei Zhang (张玉美)[14]
Zhenyu Zhang (张振宇)[25] Zhicheng Zhang (张志诚)[18] Zhijian Zhang (张志坚)[11] Jie Zhao (赵洁)[3]
Runze Zhao (赵润泽)[3,12] Shujun Zhao[28] Yangheng Zheng (郑阳恒)[7] Li Zhou (周莉)[3] Lishui Zhou[23]
Shun Zhou (周顺)[3] Xiang Zhou (周详)[25] Xing Zhou (周星)[3] Jingsen Zhu (朱景森)[14] Kangfu Zhu (朱康甫)[26]
Kejun Zhu (朱科军)[3] Bo Zhuang[3] Honglin Zhuang (庄红林)[3] Jiaheng Zou (邹佳恒)[3]

[1]Université Libre de Bruxelles, Brussels, Belgium
[2]Beijing Institute of Spacecraft Environment Engineering, Beijing, China
[3]Institute of High Energy Physics, Beijing, China
[4]New Cornerstone Science Laboratory, Institute of High Energy Physics, Beijing, China
[5]North China Electric Power University, Beijing, China
[6]Tsinghua University, Beijing, China
[7]University of Chinese Academy of Sciences, Beijing, China
[8]College of Electronic Science and Engineering, National University of Defense Technology, Changsha, China
[9]Chengdu University of Technology, Chengdu, China
[10]Chongqing University, Chongqing, China
[11]Dongguan University of Technology, Dongguan, China
[12]Kaiping Neutrino Research Center, Guangdong, China
[13]Jinan University, Guangzhou, China
[14]Sun Yat-Sen University, Guangzhou, China
[15]Harbin Institute of Technology, Harbin, China
[16]University of South China, Hengyang, China
[17]Wuyi University, Jiangmen, China
[18]Shandong University, Jinan, and Key Laboratory of Particle Physics and Particle Irradiation of Ministry of Education, Shandong University,Qingdao, China
[19]Nanjing University, Nanjing, China
[20]Guangxi University, Nanning, China
[21]School of Physics and Astronomy, Shanghai Jiao Tong University, Shanghai, China
[22]Tsung-Dao Lee Institute, Shanghai Jiao Tong University, Shanghai, China
[23]Department of Earth and Space Sciences, Southern University of Science and Technology, Shenzhen, China
[24]Nankai University, Tianjin, China
[25]School of Physics and Technology, Wuhan University, Wuhan, China
[26]Xi'an Jiaotong University, Xi'an, China

CPC Accepted

[27]Xiamen University, Xiamen, China
[28]School of Physics, Zhengzhou University, Zhengzhou, China
[29]Institute of Physics, National Yang Ming Chiao Tung University, Hsinchu
[30]National United University, Miao-Li
[31]Department of Electro-Optical Engineering, National Taipei University of Technology, Taipei
[32]Department of Physics, National Taiwan University, Taipei
[33]Charles University, Faculty of Mathematics and Physics, Prague, Czech Republic
[34]University of Jyvaskyla, Department of Physics, Jyvaskyla, Finland
[35]IJCLab, Université Paris-Saclay, CNRS/IN2P3, 91405 Orsay, France
[36]Univ. Bordeaux, CNRS, LP2I, UMR 5797, F-33170 Gradignan, France
[37]IPHC, Université de Strasbourg, CNRS/IN2P3, F-67037 Strasbourg, France
[38]Aix Marseille Univ, CNRS/IN2P3, CPPM, Marseille, France
[39]SUBATECH, Nantes Université, IMT Atlantique, CNRS/IN2P3, Nantes, France
[40]III. Physikalisches Institut B, RWTH Aachen University, Aachen, Germany
[41]Institute of Experimental Physics, University of Hamburg, Hamburg, Germany
[42]Forschungszentrum Jülich GmbH, Nuclear Physics Institute IKP-2, Jülich, Germany
[43]Institute of Physics and EC PRISMA$^+$, Johannes Gutenberg Universität Mainz, Mainz, Germany
[44]Technische Universität München, München, Germany
[45]GSI Helmholtzzentrum für Schwerionenforschung GmbH, Planckstr. 1, D-64291 Darmstadt, Germany
[46]Eberhard Karls Universität Tübingen, Physikalisches Institut, Tübingen, Germany
[47]INFN Catania and Dipartimento di Fisica e Astronomia dell Università di Catania, Catania, Italy
[48]Department of Physics and Earth Science, University of Ferrara and INFN Sezione di Ferrara, Ferrara, Italy
[49]INFN Sezione di Milano and Dipartimento di Fisica dell Università di Milano, Milano, Italy
[50]INFN Milano Bicocca and University of Milano Bicocca, Milano, Italy
[51]INFN Milano Bicocca and Politecnico of Milano, Milano, Italy
[52]INFN Sezione di Padova, Padova, Italy
[53]Dipartimento di Fisica e Astronomia dell'Università di Padova and INFN Sezione di Padova, Padova, Italy
[54]INFN Sezione di Perugia and Dipartimento di Chimica, Biologia e Biotecnologie dell'Università di Perugia, Perugia, Italy
[55]Laboratori Nazionali di Frascati dell'INFN, Roma, Italy
[56]Dipartimento di Matematica e Fisica, Università Roma Tre and INFN Sezione Roma Tre, Roma, Italy
[57]Department of Physics, National Kaohsiung Normal University, Kaohsiung
[58]Pakistan Institute of Nuclear Science and Technology, Islamabad, Pakistan
[59]Joint Institute for Nuclear Research, Dubna, Russia
[60]Comenius University Bratislava, Faculty of Mathematics, Physics and Informatics, Bratislava, Slovakia
[61]High Energy Physics Research Unit, Faculty of Science, Chulalongkorn University, Bangkok, Thailand
[62]National Astronomical Research Institute of Thailand, Chiang Mai, Thailand
[63]Suranaree University of Technology, Nakhon Ratchasima, Thailand
[64]The University of Liverpool, Department of Physics, Oliver Lodge Laboratory, Oxford Str., Liverpool L69 7ZE, UK, United Kingdom
[65]University of Warwick, Coventry, CV4 7AL, United Kingdom
[66]Department of Physics and Astronomy, University of California, Irvine, California, USA

CPC Accepted

Abstract: The Jiangmen Underground Neutrino Observatory (JUNO) collaboration has completed construction of the 20,000-ton liquid scintillator detector and the associated muon veto detector system. To achieve its physics objectives, the materials used in the detector must exhibit low levels of radioactive contamination. The single-event rate in the fiducial volume (R < 17.2 m) of the scintillator is required to be approximately 7 Hz for energies above 0.7 MeV, resulting in an accidental coincidence background of about 1 event per day for reactor neutrino physics analyses. Since the beginning of the construction phase, we have screened the natural radioactivity content of thousands of materials to select those that satisfy the design background budget. The concentrations of radioactive impurities in the materials ultimately used in the JUNO detector are summarized in this paper. Construction of the entire detector and subsequent filling with liquid scintillator were completed in August 2025. Initial data indicate that the total count rate from natural radioactivity within the detector's fiducial volume has reached nearly 5 Hz, with a 20–30% uncertainty arising from differences among reconstruction algorithms. This background level is sufficient to support the reactor antineutrino analysis.

Keywords: JUNO, Background, Natural radioactivity, reactor antineutrino

DOI: 10.1088/1674-1137/aeb48b **CSTR:**

I. INTRODUCTION

The primary physics objective of the Jiangmen Underground Neutrino Observatory (JUNO) is to determine the neutrino mass ordering and measure neutrino oscillation parameters with high precision by detecting reactor antineutrinos through the inverse beta decay reaction (IBD) [1, 2, 3]. In addition, JUNO can study neutrinos from various astrophysical sources, including the Sun, core-collapse supernovae, and the Earth. To achieve these

physics goals, the detector's intrinsic background must be sufficiently low. This background is dominated by the natural radioactivity of detector materials and cosmic-ray-induced backgrounds. The JUNO detector is constructed at a depth of about 650 m, which reduces the cosmic-ray component to a sufficiently low level. However, controlling the natural radioactive content of detector materials remains critical throughout detector design, production, and installation, requiring meticulous quality control based on dedicated radioactivity measurements. To meet JUNO's sensitivity requirement for determining the neutrino mass ordering, the background count rate, or singles rate, originating from natural radioactivity must be kept below 10 Hz [1]. This requirement also ensures the target sensitivity for supernova neutrino detection, which is also based on IBD analysis. For solar neutrino studies, however, intrinsic radioactivity dominates the background, and the requirements for LS radiopurity are more stringent and depend strongly on the contaminant type [4, 5, 6].

JUNO is the world's largest liquid scintillator (LS) detector to date; a schematic diagram of its design is shown in Figure 1, and details can be found in Ref. [2]. Twenty thousand tons of LS are contained within an acrylic sphere with an inner diameter of 35.4 m and a wall thickness of 0.12 m. The 600-ton acrylic vessel is constructed on site by assembling 263 acrylic panels layer by layer. The entire acrylic sphere is supported by an outer stainless steel (SS) structure with a diameter of 41.1 m, connected via SS support rods. The outer surface of the sphere features 590 acrylic nodes for attaching these SS support rods. The central detector (CD) consists of the acrylic vessel and the SS structure. The space outside the acrylic sphere is filled with 40,000 tons of ultrapure water, which shields against backgrounds from the surrounding rock and serves as a water Cherenkov detector (WCD).

To capture the faint light signals from neutrino interactions, 17,596 20-inch photomultiplier tubes (PMTs) and 25,587 3-inch PMTs are installed on the inner side of the SS truss. In addition, 2,399 20-inch PMTs are installed on the outer side of the SS truss to observe cosmic rays [7]. To minimize interference from long cables, the readout electronics and high-voltage modules for the PMTs are located underwater, directly adjacent to the PMTs. This arrangement requires extremely high waterproofing standards.

Magnetic shielding coils installed outside the SS truss

CPC Accepted

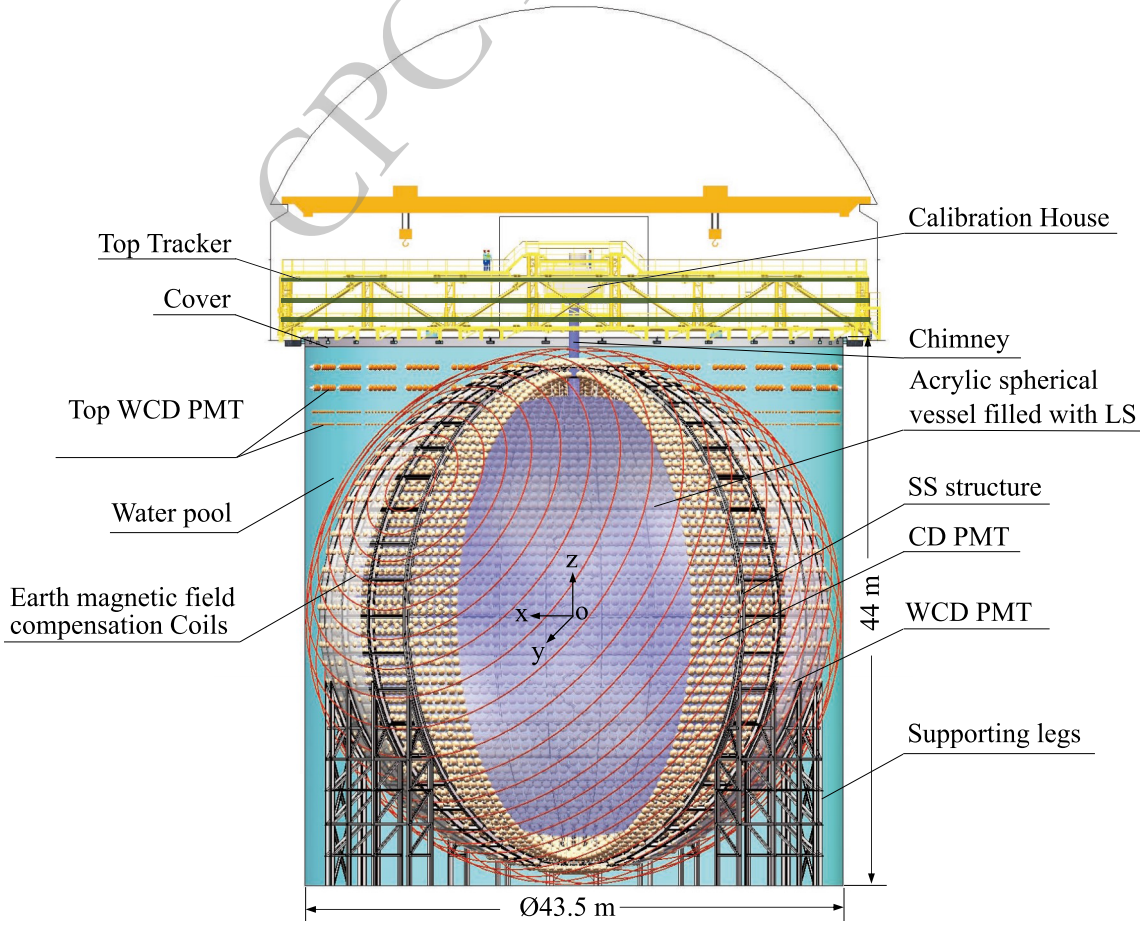

Fig. 1. Conceptual diagram of the JUNO detector.

are used to mitigate the effects of the Earth's magnetic field on the PMTs. A plastic scintillator tracker installed at the top of the detector assists the water Cherenkov detector in tagging cosmic rays. Because the LS inside the acrylic sphere and the water outside have different densities, the liquid level inside the sphere must be higher than that outside. To accommodate this requirement, a 9-m-high chimney is installed above the acrylic sphere and connects it to the calibration room at the top. This chimney serves two purposes: it allows for LS overflow caused by temperature-induced volume changes, and it facilitates the deployment of calibration sources into the detector for energy response measurements.

The energy calibration is performed using a redundant system of multiple sources, both radioactive and laser-based, and multidimensional scanning systems [8]. For a one-dimensional scan, the Automatic Calibration Unit (ACU) can deploy sources along the central axis of the detector. Off-axis calibration positions are obtained using a Cable Loop System (CLS), which can be moved within a vertical half-plane by adjusting the lengths of two connection cables. During CLS calibration, the source position can be verified using four high-resolution Charge-Coupled Device (CCD) cameras (6576×4384) mounted on the equator. These cameras locate an active light source suspended beneath the calibration source, thereby determining the source position. A Guide Tube Calibration System (GTCS) surrounds the exterior of the acrylic sphere and runs in a longitudinal loop to calibrate the nonuniformity of the energy response at the detector boundary. A source is pulled into the Teflon GTCS with servomotors to reach the desired locations. For both the CLS and GTCS, an array of eight customized low-radioactivity Ultrasonic Sensor System (USS) receivers enables reconstruction of source positions based on signals emitted by transmitters on the source attachment fixture.

The spontaneous decay of naturally occurring radioactive nuclides in detector materials emits radiation, including α, β, and γ rays, which can enter the LS and contribute to the background of neutrino events. Charged particles such as α and β emitted by materials outside the LS are strongly attenuated and rarely reach the LS, whereas neutral γ rays can penetrate into the LS and contribute to the background. As γ rays propagate through matter, their energies are progressively attenuated; therefore, stricter radioactivity control is required for materials located closer to the LS than for those farther away. Based on the JUNO software framework, we simulated natural radioactivity on the outer surface of the acrylic sphere, PMTs, and SS truss [9]. The radioactivity contributions from the PMTs and SS truss are approximately three orders of magnitude lower than that from the acrylic outer surface because of the presence of about 3 m of water shielding. The requirements for the concentrations of naturally occurring radioactive nuclides inside the LS are particularly stringent, because all decay products can deposit energy in the LS and contribute directly to the background. Based on a combination of industry-wide production capacity surveys and simulation studies, the design specifications for radioactive impurity levels in various detector materials have been defined, and the resulting event rates in the LS are summarized in Table 1

CPC Accepted

Table 1. The final background budget for the main materials used in the JUNO detector, for events with reconstructed energies greater than 0.7 MeV, is taken from Ref. [9]. The two rows for the SS structure correspond, respectively, to the SS shell positioned farther from the LS and to the SS joints and supporting bars located closer to the LS. The three rows labeled PMT glass correspond, in order, to 20-inch dynode-PMTs, 20-inch MCP-PMTs, and 3-inch PMTs. The two rows under PMT readout correspond to the readout electronics for the 20-inch and 3-inch PMTs, respectively. The expected count rates are reported for both the full detector volume (R = 17.7 m) and the default fiducial volume (R = 17.2 m).

Material	Mass [t]	Target impurity concentration					Singles	
		^{238}U [10^{-9} g/g]	^{232}Th[10^{-9} g/g]	^{40}K[10^{-9} g/g]	^{210}Pb[10^{-9} g/g]	^{60}Co[mBq/kg]	DV[Hz]	FV[Hz]
LS-reactor	20000	10^{-6}	10^{-6}	10^{-7}	10^{-13}		2.5	2.2
Acrylic	610	10^{-3}	10^{-3}	10^{-3}			8.4	0.4
SS structure	1000	1	3	0.2		20	15.9	1.1
	65	0.2	0.6	0.02		1.5		
PMT glass	33.5	400	400	40			26.2	2.8
	100.5	200	120	4				
	2.6	400	400	200				
PMT readout	125	68	194	5		16	3.4	0.4
	16.3	93	243	12		14		
Other							2.5	0.3
Sum							59	7.2

Table 2. The table compares the advantages and disadvantages of the three detection methods. The sensitivity range and testing time depend on the sample type.

	HPGe	NAA	ICP-MS
Nuclei	^{238}U, ^{226}Ra, ^{228}Ra,^{228}Th, ^{40}K, ^{60}Co	^{238}U, ^{232}Th, ^{40}K, ^{85}Kr	^{238}U, ^{232}Th
Destructive testing	No	Yes/No	Yes
Decay chain equilibrium check	Yes	No	No
Treatment	No	Simple	Complex
Sample mass [kg]	0.1-20	0.001-0.05	0.001-0.01
Sample mass with enrichment [kg]	-	0.05-2	0.1-10
Sensitivity	(0.1-100) mBq/kg	(10^{-12}-10^{-16}) g/g	(10^{-12}-10^{-17}) g/g
Time [day]	1-30	10-30	2-5

[9]. The table shows the target impurity concentrations for ^{238}U, ^{232}Th, ^{40}K, ^{210}Pb, and ^{60}Co. The simulation assumes that the uranium and thorium decay chains are in secular equilibrium. In the first row, *LS-reactor* refers to the minimum radiopurity requirements for the LS to accomplish the primary physics objectives of JUNO using reactor antineutrinos. The simulated event rates reported in the last two columns of the table correspond, respectively, to the entire detector volume (DV) and to a fiducial volume (FV) with radius R < 17.2 m, for energies above 0.7 MeV. In the table, rows for the same material are subcategorized into separate entries. This accounts for contributions from materials deployed at various locations and from different types of PMTs. Even for the same material type, the background contribution can vary depending on the installation position. The background levels of products manufactured by different PMT manufacturers vary significantly; therefore, these are listed in distinct rows. In the "Other" row, several minor contributors are grouped together. These include calibration components and cables installed on the inner surface of the acrylic sphere (0.12 Hz), water from the Cherenkov detector (0.06 Hz), and the rock wall (0.13 Hz). Notably, the water in the WCD is required to have a U/Th content better than 10^{-14} g/g, a ^{222}Rn concentration better than 10 mBq/m^3, and a ^{226}Ra concentration better than 1 mBq/m^3. For the filling water and the water extraction system, the required radiopurity must be 1–2 orders of magnitude better than that of the WCD water. Specifically, for the filling water, which contacts only the surface of the LS, the radiopurity is required to be one order of magnitude better than that of the WCD water. In contrast, for the water extraction system used to purify the LS, the water is fully mixed with the LS; therefore, its radiopurity must be two orders of magnitude better than that of the WCD water.

To achieve the objectives outlined in Table 1, we meticulously screened thousands of samples during the selection and production of detector raw materials. Finally, those with the lowest levels of natural radioactivity were selected for the construction of JUNO.

The paper is organized as follows. Section 2 provides a brief overview of the screening facilities and instrumentation within the collaboration used to quantify the radiopurity of detector components. Section 3 summarizes the measurement results for all raw materials used in the JUNO detector. Section 4 presents results from initial detector data and compares them with the design expectations. Finally, Section 5 summarizes this research.

II. SCREENING EQUIPMENT RESOURCES

The methods commonly used to measure natural radioactivity (U, Th, K) in materials primarily include three techniques: high-purity germanium (HPGe) gamma spectrometry, neutron activation analysis (NAA), and inductively coupled plasma mass spectrometry (ICP-MS). Each detection method has its own advantages and limitations, and their main performance characteristics are compared in Table 2. The sensitivity is expressed in Bq/kg or in mass concentration units [1)] (g/g, i.e., grams of contaminant per gram of material). For a few acrylic samples, U/Th surface contamination was also measured by laser ablation ICP-MS (LA-ICP-MS). To ensure that the radon level in the water is as low as possible, several facilities for radon emanation and radon permeability measurements were used. A detailed description of the screening facilities used for JUNO samples is provided in Ref. [9], to which we refer for further details. In practical measurements, the appropriate analytical method is selected based on a comprehensive consideration of the design specifications and the strengths and limitations of the available techniques. For particularly critical components, multiple methods may be applied.

1) For convenience, the conversions between the two units used in this paper are provided: 1 mBq of ^{232}Th activity per kg of material is equivalent to a ^{232}Th mass concentration of 2.5×10^{-10} g/g in that material. Similarly, 1 mBq of ^{238}U corresponds to 8.1×10^{-11} g/g of ^{238}U, and 1 mBq/kg of ^{40}K corresponds to 3.8×10^{-12} g/g of ^{40}K, equivalent to 3.2×10^{-8} g/g of natural K.

CPC Accepted

Compared with the instrumentation and sensitivity reported in Ref. [9], our quality inspection capabilities have been further enhanced. For LS screening, novel methods have been developed for both ICP-MS and NAA. These methods extract U/Th from the LS using nitric acid and subsequently concentrate the acid solution. For ICP-MS, after 3–5 days of experimental processing, the measurement sensitivity for U/Th can reach 10^{-16}–10^{-17} g/g [10]. This technique has been extensively applied in the quality assurance/quality control (QA/QC) processes during LS production and filling for JUNO. For NAA, after the pre-concentration step and neutron irradiation, radiochemical separation combined with $\beta-\gamma$ coincidence spectroscopy was implemented, allowing sensitivities for U/Th in the range of 10^{-15}–10^{-16} g/g [11]. For K, no pre-concentration step is required; only radiochemical separation is performed after neutron irradiation of the LS, followed by gamma spectroscopy. This method achieves sensitivities at the level of 10^{-16} g/g [12].

For radiopurity measurements of acrylic samples, we have developed a rapid and sensitive method to quantify ^{238}U and ^{232}Th below 10^{-12} g/g within 2–3 days, based on microwave ashing coupled with ICP-MS analysis [13]. Compared with the previous approach [14], this method is significantly simpler, safer, and more efficient. It has been extensively implemented in the QA/QC procedures (described in Section 3.1) during the production and surface treatment of acrylic components for the JUNO experiment. Cross-check measurements using NAA and the method described in [15] have been performed periodically.

We have significantly improved the sensitivity of our instrumentation for measuring radon levels in both gas and water. The achieved sensitivities reach 0.26 μBq/m^3 for radon measurements in nitrogen [16] and 0.6 mBq/m^3 for radon measurements in water [17]. In addition, by using manganese wire to concentrate radium in water and coupling it with radon detection devices, we have developed a method capable of measuring radium concentrations in water down to 6 μBq/m^3 [18]. This method has been used for quality control of ultrapure water in JUNO.

III. Screening results

In this section, the quality inspection results for all detector materials that meet the JUNO requirements are systematically summarized by detector subsystem, following the categories listed in Table 1. These results were obtained from several years of screening activities, during which only materials with sufficiently low contaminant concentrations were retained. Because different analytical techniques probe different radionuclides in the natural ^{238}U and ^{232}Th decay chains, the quality control results are organized accordingly. Measurements of the parent radionuclides obtained using ICP-MS and NAA are presented separately from results based on the assumption of decay-chain equilibrium, which are derived from HPGe spectrometry. When a sample is annotated with "(XX batches)", the reported result corresponds to the average of multiple production batches. Results without this notation are based on a single measurement. For critical materials, multiple batches were screened to ensure consistency.

A. Screening by ICP-MS and NAA

These two techniques were used for materials whose radiopurity is critically important, requiring screening of ^{238}U and ^{232}Th concentrations well below 10^{-12} g/g. This requirement applies to all materials very close to or in direct contact with the LS, including the LS itself, as listed in Table 3. For ICP-MS screening of water and LS, sample enrichment is required, and the processed sample mass typically ranges from 0.1 to 10 kg, depending on the target sensitivity. In contrast, other material samples analyzed by ICP-MS generally require only a few grams and do not undergo an enrichment step. For NAA, sample masses on the order of 10–50 g were irradiated directly for organic matrices, whereas LS samples required pre-concentration, with processed masses up to 2 kg.

The final JUNO LS mixture consists of four components at different concentrations. The base solvent is linear alkylbenzene (LAB), doped with 2.5 g/L of 2,5-diphenyloxazole (PPO) as the primary fluor, 3 mg/L of 1,4-bis(2-methylstyryl)benzene (bis-MSB) as the wavelength shifter, and 42.7 mg/L of butylated hydroxytoluene (BHT) as the antioxidant. Table 3 reports the radiopurity screening results for the individual components. The LS mixture was prepared and purified directly at the JUNO site [2]. The raw LAB produced by SINOPEC first undergoes alumina (Al_2O_3) filtration to reduce optical impurities and is subsequently processed in a distillation plant [19] to remove heavy contaminants. The mixing system then produces the LS cocktail, which is further purified underground by water extraction to remove heavy metals and by gas stripping [19] to eliminate volatile impurities. The purified LS is finally stored in the Filling and Overflow Control (FOC) system before being transferred into the acrylic vessel. During LS production for JUNO, samples were taken regularly after each purification step to monitor and validate the radiopurity. The results obtained by ICP-MS [10] are summarized in Figure 2. The screening results from the distillation system during commissioning were consistently below the ICP-MS detection limit. Therefore, samples from stages up to and including distillation were analyzed only at the beginning of production, whereas subsequent samples were taken from later stages (mixing, water extraction, gas stripping, and FOC systems) to optimize the use of measurement resources. For the water extraction system, an initial cleanliness issue was identified at the start of production. Con-

CPC Accepted

Table 3. This table lists the JUNO samples analyzed using the destructive analytical methods ICP-MS and NAA. The upper limits for most materials listed in the table are reported at 95% C.L., whereas those for calibration components are reported at 90% C.L.

Type	Material	Producer	Mass for JUNO	Technique	^{238}U [10^{-12} g/g]	^{232}Th [10^{-12} g/g]	^{40}K [10^{-12} g/g]
LS	LAB (37 batches)	SINOPEC, Nanjing, China	20,000 t	ICP-MS	$(0.6\pm0.1)\times10^{-3}$	$(1.0\pm0.1)\times10^{-3}$	-
	PPO (19 batches)	HAISO, Wuhan, China	60 t	ICP-MS	0.09±0.02	0.07±0.02	-
	PPO (2 batches)		60 t	NAA	<0.3	<0.5	1.24±0.03
	BHT (2 batches)		1 t	ICP-MS	0.14±0.03	0.07±0.04	-
	BHT		1 t	NAA	<3.0	<3.0	3.8±0.2
	bis-MSB (3 batches)		72 kg	ICP-MS	2.9±0.1	2.0±0.1	-
Water	Final LS	JUNO	20,000 t	ICP-MS	$<3.4\times10^{-5}$	$<3.3\times10^{-5}$	-
	Final LS		20,000 t	NAA	$<6.5\times10^{-4}$	$<1.8\times10^{-3}$	$<2\times10^{-4}$
	For water-extraction		6,700 t	ICP-MS	$<2.6\times10^{-4}$	$<1.0\times10^{-5}$	
	For detector filling	JUNO	23,200 t	ICP-MS	$(4\pm1)\times10^{-4}$	$<4\times10^{-4}$	
	For water Cherenkov detector		40,000 t	ICP-MS	$(5\pm1)\times10^{-4}$	$<4\times10^{-4}$	
	Filled CD water surface		-	ICP-MS	$(1.05\pm0.06)\times10^{-3}$	$(3.7\pm0.7)\times10^{-4}$	
Organic materials	Acrylic panels (44 batches)	Donchamp, Taixing, China	600 t	ICP-MS	0.62±0.05	0.72±0.05	-
	Acrylic panels (13 batches)	Donchamp, Taixing, China	600 t	NAA	<0.2	<0.1	0.1-0.4
	Acrylic surface (~10 μm)	-	-	ICP-MS	15.2±0.7	24.3±0.7	-
	Acrylic subsurface (~65-75 μm)	-	-	LA-ICP-MS	3.9±0.6	6.8±0.8	-
	PMT acrylic cover	Huashuaite, Jiaxing, China	110 t	ICP-MS	3.1±0.3	10±1	-
	Teflon in acrylic node	BMC, Kunshan, China	300 kg	NAA	16±2	82±5	283±11
	Epoxy (type 8010) for acrylic bonding line	DODI, Shanghai, China	3 kg	ICP-MS	<5	<7	-
	Water-soluble glue on film	Elleair, Japan	-	ICP-MS	450±20	115±6	-
	Calibration CLS anchors, PTFE	Sanxin Inc., China	6.3 kg	NAA	<1.2	10±2	1.50±0.05
	Calibration wear-resisting blocks, PTFE	Sanxin Inc., China	6.9 kg	NAA	<1.2	10±2	1.50±0.05
	Calibration GTCS Tube, PTFE	Jianwei, China	20 kg	NAA	<1.65	<3	470±10

CPC Accepted

sequently, this system was used only after its cleanliness had been confirmed by ICP-MS, and it became operational on March 25, 2025. Most of the screening results shown in the figure were below the ICP-MS detection limit. In June and July 2025, some FOC system screening points yielded measured contaminant concentrations rather than upper limits, whereas the gas stripping samples provided only upper limits. This discrepancy is tentatively attributed to possible sampling contamination, although it has not been conclusively verified. Table 3 summarizes the average LS screening results from the FOC system, obtained after all purification steps defined by the JUNO protocol [2] and before detector filling.

Water is another crucial material for the JUNO detector. In addition to being the main component of the water Cherenkov detector, it was used in the water-extraction purification step [19] for the LS and in the *water-exchange* filling procedure [7] adopted to fill the JUNO detector. After filling the acrylic sphere with ultrapure water (UPW), we collected surface water samples from the top chimney. Extensive measures were implemented to ensure detector cleanliness [20], and this measurement serves as an indicator of both the internal environment and the cleanliness of the acrylic surface. The results for the different samples are reported in Table 3, and all samples meet the filling water requirement of U/Th$<10^{-15}$ g/g. This indicates that both the internal environment of the acrylic vessel and its surface remained very clean after installation. The ^{222}Rn and ^{226}Ra activities in water were measured using the methods described in Refs. [17, 18]. For the water extraction system, the measured ^{222}Rn activity in UPW was below 1 mBq/m^3, while for the water Cherenkov detector it was below 10 mBq/m^3. The ^{226}Ra activity in UPW was below 10 μBq/m^3 for both the water Cherenkov detector and the water extraction system.

The acrylic vessel, as anticipated in Section 1, was constructed on site by bonding 263 acrylic panels layer by layer. All batches of acrylic panels were screened by ICP-MS to verify their radiopurity; the results are shown

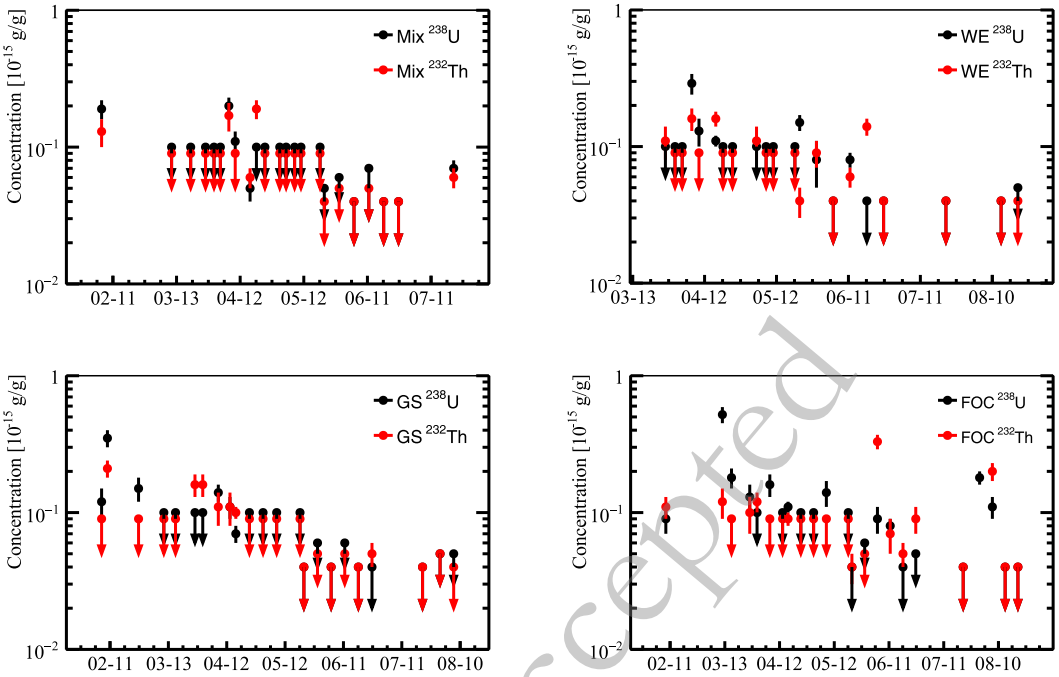

Fig. 2. Time evolution of the ICP-MS screening results for U/Th concentrations in LS during the filling of the JUNO detector in the first half of 2025. Top left: "MIX" denotes the mixing system. Top right: "WE" denotes the water extraction system. Bottom left: "GS" denotes the gas stripping system. Bottom right: "FOC" denotes the filling and overflow control system.

CPC Accepted

in Figure 3, and the average values are summarized in Table 3. After production, the panels were stored temporarily at the manufacturer's facility, with their surfaces protected by a polyethylene (PE) film. LA-ICP-MS measurements revealed that the radioactive contamination in the top 50 μm of the surface could be 2–3 orders of magnitude higher than that in the bulk material. Therefore, it was decided to remove at least 100 μm from the surface before shipment to the JUNO site.

Following a detailed study of potential background contamination during the surface-treatment process, the final procedure was implemented for the JUNO acrylic-panel production [13]. In Table 3, *acrylic surface* refers to surface scrapings from a specified thickness of the acrylic panels, measured to assess the residual radioactive contamination after surface polishing. After careful surface treatment, each panel was covered with a water-soluble paper film to protect it from dust and the implantation of radon daughters until detector filling. Moreover, each bond line was sealed with a special epoxy to prevent chemical reactions with the LS during long-term operation. Acrylic covers were also manufactured to protect the glass of the 20-inch PMTs from chain explosions—a phenomenon in which the explosion of one PMT generates a shock wave in water that triggers the explosion of adjacent PMTs, resulting in a chain reaction.

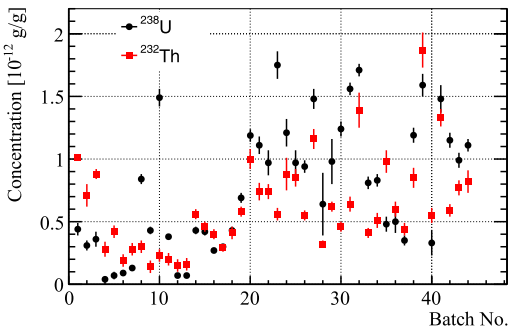

Fig. 3. Evolution of ICP-MS screening results for U/Th concentrations in acrylic during the production of panels for the acrylic vessel.

B. Screening by HPGe

For HPGe detectors, only gamma-ray lines from the decay daughters of the ^{238}U and ^{232}Th chains—starting from ^{226}Ra and ^{228}Ra onward—can be measured. At sufficiently high concentrations of ^{238}U, γ-ray lines from ^{234}Th and ^{234m}Pa may also be observed. However, in our background simulations, we assume secular equilibrium throughout the entire decay chains. The gamma spectrometers used for material screening in JUNO are HPGe detectors protected by passive and/or active shielding and located in several underground laboratories worldwide (China Jinping Underground Laboratory (CJPL) in China, Laboratoire Souterrain de Modane (LSM) in France, and Laboratori Nazionali del Gran Sasso (LNGS) in Italy) or in sea-level laboratories (IHEP in China, LP2i Bordeaux in France, and UNIMIB in Italy). The sample mass ranges from 0.1 to 15 kg, depending on the geometry and density of the material.

A system-by-system overview of the HPGe quality

screening for JUNO materials is presented in Tables 4–8. Owing to the limited sensitivity to ^{60}Co at the level of 10 mBq/kg, screening results for this isotope obtained at IHEP are not included.

Table 4 reports the HPGe screening results for most of the materials used to build the central detector (CD) and the LS purification system, namely the LS, the acrylic vessel, the SS truss, and the supporting rods. The LS and FOC measurements refer to the stainless steel used for the LS purification system and the FOC system [2], i.e. all pipes and tanks employed for LS filling and level control in the detector.

Table 5 reports the HPGe screening results for most of the materials used in the calibration system, namely the USS, CLS, GTCS, and CCD.

Table 6 reports the HPGe screening results for the main materials used in the PMT system, namely the glass bulb, the potting materials, and the voltage divider components. Of the nearly 20,000 20-inch PMTs deployed in the JUNO detector, approximately 5,000 were dynode-PMTs procured from Hamamatsu, while the remaining 15,000 were MCP-PMTs supplied by NNVT. The glass envelopes for the MCP-PMTs were manufactured in China, providing an opportunity for close collaboration with the supplier to optimize the production line. The production of the PMT bulbs required extensive screening of low-background raw materials and careful control of potential secondary contamination introduced during manufacturing from the environment, tools, or contact materials. To mitigate these effects, a dedicated background control program was implemented at the manufacturer's site, including on-site supervision by members of the collaboration and the optimization of cleanliness procedures throughout the production chain [21]. These measures significantly reduced the U, Th, and K contents of the MCP-PMT glass, reaching levels comparable to the best values reported for large photomultiplier tubes. During mass production, representative batches of bulbs were

CPC Accepted

Table 4. This table lists the CD- and LS–related samples analyzed using non-destructive HPGe assay methods. The upper limits reported in this table are given at 95% C.L., except for the LNGS measurements, which are quoted at 68% C.L.

CD and LS	Material	Producer	Mass for JUNO	Screening	^{226}Ra [Bq/kg]	^{228}Ra [Bq/kg]	^{40}K [Bq/kg]	^{60}Co [mBq/kg]
LS	PPO	HAISO, Wuhan, China	60 t	UNIMIB	<0.2	<0.03	<0.3	<0.01
	Al_2O_3	SHAN LV YI FENG, Zibo, China	300 t	IHEP	0.26±0.03	<0.22	<0.70	-
Acrylic node	Bulk, SS304 (2 batches)	TISCO, Taiyuan, China	24 t	CJPL	$<4\times10^{-3}$	$(2.8\pm0.7)\times10^{-3}$	<0.05	0.7±0.3
	Bolt, SS304			CJPL	$(7\pm5)\times10^{-3}$	$(8\pm2)\times10^{-3}$	0.05±0.04	2±1
	Solder Φ1.2, SS308	Golden Bridge, Tianjin, China	4.5 t	IHEP	0.39±0.08	0.15±0.10	2.4±0.5	-
Support rod	Bulk, SS304 (8 batches)	TISCO, Taiyuan, China	67 t	CJPL	$<4\times10^{-3}$	$(2\pm1)\times10^{-3}$	0.05±0.03	2.0±0.7
	Bulk, SS304		67 t	LNGS	$(0.3\pm0.1)\times10^{-3}$	$(0.8\pm0.3)\times10^{-3}$	$<2.8\times10^{-3}$	$(0.4\pm0.1)\times10^{-3}$
SS truss	Bulk, SS304 (17 batches)		608 t	CJPL	$(6\pm2)\times10^{-3}$	$(3\pm1)\times10^{-3}$	$(4\pm2)\times10^{-3}$	1.4±0.5
	Bulk, SS304		608 t	LP2IB	$<1.1\times10^{-3}$	$(4.7\pm0.7)\times10^{-3}$	$<9\times10^{-3}$	0.50±0.15
	Bolt, SS630, SS	TISCO, Taiyuan, China	65 t	CJPL	$<4\times10^{-3}$	$(6\pm3)\times10^{-3}$	0.17±0.07	10±3
	Ring gasket, SS			CJPL	$<4\times10^{-3}$	$(1.5\pm0.7)\times10^{-2}$	0.3±0.1	11±2
	Spring, SS		10 t	IHEP	<0.11	<0.06	<0.35	-
	Paint, SS	NIMTE, Ningbo, China		CJPL	$(2.4\pm0.7)\times10^{-2}$	$(1.9\pm0.3)\times10^{-2}$	0.43±0.05	3±2
	Solder Φ3.2, SS308	Golden Bridge, Tianjin, China	8.9 t	IHEP	0.17±0.07	0.21±0.06	<1.3	-
Chimney	Bulk, SS304			IHEP	<0.12	<0.15	<0.6	-
	Bellow, SS304	TISCO, Taiyuan, China		CJPL	$(8\pm5)\times10^{-3}$	$<5\times10^{-3}$	0.04±0.03	12±2
	Bolt, SS304		48 kg	CJPL	$(1.3\pm0.7)\times10^{-2}$	$(4\pm2)\times10^{-3}$	0.09±0.05	11±2
LS and FOC	Tank and pipes, SS316 (2 batches)	TISCO, Taiyuan, China	50 t	CJPL	$<4\times10^{-3}$	$(6\pm2)\times10^{-3}$	0.09±0.05	3±2
Acrylic Vessel	Acrylic sample	Donchamp, Taixing, China	600 t	LNGS	$<45\times10^{-6}$	$<62\times10^{-6}$	$<0.3\times10^{-3}$	-
Acrylic surface treatment	Sanding paper	Anda, Taixing, China	10^6 pieces	IHEP	<0.5	<0.4	<1.9	-
	PE film	Baojiali, Nantong, China	10^5 m^2	IHEP	<0.23	<0.15	<0.9	-
	Protection paper film	Daio Paper Corporation, Japan	10^4 m^2	IHEP	<0.5	0.6±0.2	<1.6	-

Table 5. This table lists the JUNO calibration-related samples analyzed using the non-destructive HPGe testing method. The upper limits reported in this table are given at 90% C.L.

Calibration	Material	Producer	Mass for JUNO	Screening	^{226}Ra [Bq/kg]	^{228}Ra [Bq/kg]	^{40}K [Bq/kg]	^{60}Co [mBq/kg]
USS	Cables (PTFE, copper)	Pasterneck, USA	1.45 kg	CJPL	$(3.4\pm0.5)\times10^{-3}$	$(1.9\pm0.5)\times10^{-3}$	$(1.7\pm0.4)\times10^{-2}$	<0.4
	Receiver (Ni, epoxy, PCB)	Customized, China	10 pieces	CJPL	<3.3 mBq/piece	<2.8 mBq/piece	<19 mBq/piece	<0.86 mBq/piece
CLS	Cables (PTFE, SS)	Fengshuo, China	0.27 kg	CJPL	<0.06	<0.08	<0.5	<38
GTCS	Cable (PTFE, SS)	Fengshuo, China	0.33 kg	CJPL	<0.04	<0.04	<0.14	$(2.9\pm0.1)\times10^{2}$
	Sensor (SS, PVC, PBT)	Omron, Japan	10 pieces	CJPL	(111±3) mBq/piece	(184±5) mBq/piece	(383±21) mBq/piece	<2.9 mBq/piece
CCD	Camera	OPT, Dongguan, China	4.4 kg	IHEP	0.7±0.3	3.3±0.4	12±2	-
	Cable	Fanya, Zhongshan, China	0.01 t	IHEP	<0.36	<0.27	<1.4	-
	Fibre-optical	HongXin, Dongguan, China	0.4 t	IHEP	<0.3	<0.17	<1.0	-

CPC Accepted

periodically screened by HPGe to verify their radiopurity, and the average results are summarized in the table. Since all PMTs and their associated electronics are operated underwater, the waterproof encapsulation at the PMT rear end must meet extremely high standards. The measurement data for these potting materials are compiled in the "Potting" section.

Table 7 reports the HPGe screening results for most of the materials used in the electronics system, including the housing, heat dissipation structure, high-voltage module, Global Control Unit (GCU) board, front-end board for 3-inch PMTs, as well as the cables and waterproof flexible conduits that run from the PMT back-end to the dry electronics racks in the experimental hall.

Table 8 reports the HPGe screening results for most of the materials used in the veto system, including the geomagnetic-field compensation coils, the high-density polyethylene (HDPE) used to prevent the diffusion of radon from rock strata and groundwater, and the truss column base structure fixed at the bottom of the pool.

C. Screening by Radon facilities

Radon in the ^{238}U chain is a radioactive noble gas that can diffuse through barriers or emanate from JUNO materials immersed in the water pool. The JUNO requirement for the radon activity concentration in the water pool is 10 mBq/m^3. To prevent radon from rock and groundwater from diffusing into the ultrapure water, a 5-mm-thick HDPE layer was installed against the rock surface. The shielding effectiveness can be evaluated based on the permeability of radon through HDPE (so-called transparency). This transparency is determined by placing a radon source on one side of the HDPE and measuring the radon concentration on the opposite side to calculate the radon penetration ratio. The transparency of a 5-mm-thick HDPE liner has been measured with a dedicated apparatus in two configurations: one with air on both sides of the HDPE liner and one with water on one side and air on the other, which is more representative of JUNO. The results are given in Table 9. The presence of water is observed to increase the radon transparency by a factor of 5–6. Nevertheless, the 5-mm-thick HDPE layer remains effective at blocking radon from the rock side under water-filled conditions.

Table 10 lists the JUNO samples screened by radon emanation measurements in nitrogen, including the bare 20-inch and 3-inch PMTs and the HDPE liner. Further details of the setup are provided in [22].

D. Concentration of ^{14}C in LAB

The radionuclide ^{14}C is an important background source in the low-energy region relevant to solar neutrino analyses. In addition, its high decay rate can cause pile-up with other physics events within a single readout window, degrading the energy resolution and thereby substantially affecting reactor antineutrino measurements. For these reasons, the ^{14}C concentration was measured in several LAB samples, including those produced for the JUNO experiment. The detector used for this purpose is located in the JUNO underground laboratory (650 m.w.e.) and is surrounded by a multilayer passive shield consisting of acid-cleaned oxygen-free high-conductivity (OFHC) copper, lead, 1 cm of HDPE, and 60 cm of borated polyethylene for neutron attenuation. The entire setup is enclosed in a light-tight, radon-suppressed environment maintained by a continuous purge of high-purity nitrogen (>100 L/h). The system employs 0.86 kg of LS contained in a 1-L transparent acrylic vessel (76 mm inner diameter, 2 mm wall thickness), viewed by two low-radioactivity Hamamatsu R1140-20 PMTs. These PMTs have a quantum efficiency of 35% at 420 nm and a U/Th radiopurity of approximately 1 mBq per PMT. A coincidence

Table 6. This table lists the JUNO PMT-related samples analyzed using the nondestructive HPGe testing method. The reported upper limits are given at the 95% C.L.

PMT	Material	Producer	Mass for JUNO	Screening	^{226}Ra [Bq/kg]	^{228}Ra [Bq/kg]	^{40}K [Bq/kg]	^{60}Co [mBq/kg]
Bulb	Module, SS304 (3 batches)	JISCO, Gansu, China	300 t	CJPL	<0.01	$<2\times10^{-3}$	<0.03	<1.5
	20-inch PMT cover, SS304 (3 batches)		150 t	CJPL	<0.01	$<5\times10^{-3}$	<0.03	<3
	20-inch MCP-PMT (10 batches)	Huida, Yancheng, China	90 t	IHEP	1.9±0.2	0.6±0.2	<1.4	-
	20-inch dynode-PMT (6 batches)	Hamamatsu, Japan	30 t	IHEP	5.3±0.2	1.4±0.3	1.7±0.2	-
	20-inch dynode-PMT		30 t	LP2IB	6.5±0.2	2.3±0.1	1.9±0.3	-
	20-inch dynode-PMT		30 t	UNIMIB	5.4±0.2	1.9±0.1	1.7±0.3	-
	3-inch PMT (8 batches)	Zhanchuang, Hainan, China	2.6 t	IHEP	2.2±0.2	1.7±0.2	29±2	-
	3-inch PMT		2.6 t	LP2IB	2.7±0.2	2.8±0.2	32±2	-
	20-inch PMT shell, SS304 (2 batches)	JISCO, Gansu, China	10 t	CJPL	$<6\times10^{-3}$	$(5\pm3)\times10^{-3}$	0.06±0.02	0.9±0.5
Potting	3-inch PMT shell, ABS	Kemei, Ningbo, China	6.4 t	IHEP	<0.32	<0.22	8.2±0.9	-
	Putyl tape (type HM36)	AECC BIAM, Beijing, China	5.7+2.5 t	IHEP	2.2±0.2	0.4±0.1	<1.5	-
	20-inch PMT Epoxy (type 8101R)	DODI, Shanghai, China	2.8 t	IHEP	0.30±0.04	0.08±0.03	<1	-
	3-inch PMT Epoxy (type 4412)	Buffle, Beijing, China	0.5 t	IHEP	<0.2	0.39±0.06	<0.6	-
	Polyurethane (type 6127)	Buffle, Beijing, China	15+2 t	IHEP	<0.29	<0.21	<1.2	-
	Shrinkable tube	WOER, Shenzhen, China	2.5+0.5 t	IHEP	<0.27	<0.18	<0.9	-
Divider	20-inch PMT PCB	-	-	IHEP	15±1	19±2	17±5	-
	20-inch PMT capacitors	Vishay, USA	-	IHEP	131±5	18.8±0.9	3±1	-
	20-inch PMT resistors	Vishay, USA	-	IHEP	2.0±0.2	2.1±0.2	10±1	-
	Divider for MCP-PMT	TJcentre, Tianjin, China	0.44 t	IHEP	34±3	15±3	<22	-
	Divider for dynode-PMT	TJcentre, Tianjin, China	0.16 t	IHEP	36±4	19±3	21±11	-
	3-inch PMT PCB	-	0.11 t	IHEP	35±2	38±2	52±3	-
	3-inch PMT chip resistors	Viking, Taiwan, China	-	IHEP	1.4±0.2	2.3±0.2	2.0±0.8	-
	3-inch PMT PCB+resistors	-	0.11 t	LP2IB	31±3	31±2	29±4	-
	3-inch PMT capacitors	Murata, Japan	0.04 t	IHEP	13.6±0.6	5.6±0.5	4±1	-
	3-inch PMT capacitors	Murata, Japan	0.04 t	LP2IB	12.2±2.2	5.8±1.3	<5.5	-
	Divider for 3-inch PMT	Juyingdianlu, Shenzhen, China	0.25 t	IHEP	29±1	34±2	42±3	-

CPC Accepted

trigger–set at a threshold of approximately 1 photoelectron (p.e.) with a 44 ns time window–is used to suppress dark noise and accidental background events. The key results obtained with this setup are summarized in Table 11. The systematic uncertainty of 20% is dominated by the detector configuration and light yield.

IV. FIRST JUNO DATA

JUNO completed detector construction and LS filling on August 26, 2025, and officially began data collection [7]. In this study, we analyzed the event distribution in the LS using data collected from October 1, 2025, to March 18, 2026, beginning approximately one month after filling was completed. The total live time of the dataset is 140 days. By this stage, radon introduced during the filling operations had decayed to a nearly constant background level. Vertex and energy reconstruction for all events follows the procedure detailed in Ref. [7], with several post-publication refinements incorporated. The resulting position reconstruction bias is constrained to within 10 cm, and the measured energy resolution is 3.4% at 1 MeV using the ^{68}Ge calibration source.

Our objective is to extract the event rate originating from natural radioactivity using experimental data, which requires excluding contributions from non-radioactive events as thoroughly as possible. Simulations indicate that radioactive events typically have energies below approximately 5 MeV. In contrast, cosmic muons have much higher energies. As they traverse the detector, they produce large numbers of secondary particles, some of which may deposit energy in the same low-energy range and thus contaminate the radioactive event sample. Therefore, in this analysis, a single event is defined as an

Table 7. This table lists the JUNO electronics-related samples analyzed using the non-destructive HPGe testing method. The upper limits reported in this table are given at 95% C.L.

Electronics	Material	Producer	Mass for JUNO	Screening	^{226}Ra [Bq/kg]	^{228}Ra [Bq/kg]	^{40}K [Bq/kg]	^{60}Co [mBq/kg]
Common materials for all PMTs	SS shell	GL, Kunshan, China	78+6.2 t	IHEP	<0.11	<0.07	0.3±0.2	-
	Shrinkable tube	WOER, Shenzhen, China	0.6 t	IHEP	<0.17	<0.14	<0.5	-
	Thermal gel	GLPOLY, Shenzhen, China	3.5+0.06 t	IHEP	0.83±0.08	0.27±0.06	<0.7	-
	Thermal copper	Futelang, Suzhou, China	15 t	IHEP	<0.05	<0.03	<0.2	-
	Back-end cable	Fanya, Zhongshan, China	68 t	IHEP	<0.18	<0.12	<0.6	-
	Back-end below	Taihe, Wuhu, China	72 t	IHEP	<0.21	<0.13	<0.8	-
20-inch PMTs	HVB PCB	GDM, Shanghai, China	0.20 t	IHEP	10±1	18±2	17±6	-
	HVB metal box (Al)	Juchuangli, Shenzhen, China	0.22 t	IHEP	<0.17	<0.10	<0.49	-
	Entire HVB	SCC, Shenzhen, China	0.9 t	IHEP	3±1	5±1	<18	-
	GCU board	SCC, Shenzhen, China	1.9 t	IHEP	8.8±0.5	12.0±0.7	13±1	-
	Cooling appendix (copper)	Futelang, Suzhou, China	0.6 t	IHEP	<0.1	<0.07	<0.3	-
	Front-end cable	Fanya, Zhongshan, China	1.7 t	IHEP	0.9±0.4	0.5±0.3	<8	-
	Front-end below (SS)	Taihe, Wuhu, China	4.4 t	IHEP	0.11±0.05	<0.10	0.4±0.3	-
3-inch PMTs	HV splitter board	SCC, Shenzhen, China	0.4 t	LP2IB	13.8±1.1	17.1±1.2	16.9±3.0	-
	GCU board		0.07 t	LP2IB	6.0±0.3	7.1±0.4	46.4±6.1	-
	ABC front-end board	FEDD, Agôn Electronics, France	0.07 t	LP2IB	6.7±0.5	9.3±0.5	5.3±1.1	
	Front-end cable	Axon, Foshan, China	1.4 t	LP2IB	$(5.6\pm1.7)\times10^{-3}$	$<4.2\times10^{-3}$	$<25\times10^{-3}$	<1
	Connector+Front-end cable	Axon, Foshan, China	2.8 t	IHEP	0.8±0.3	1.0±0.3	<1.8	

Table 8. This table lists the JUNO veto-related samples analyzed using non-destructive HPGe testing methods. The upper limits reported in this table are at the 95% C.L.

Veto	Material	Producer	Mass for JUNO	Screening	^{226}Ra [Bq/kg]	^{228}Ra [Bq/kg]	^{40}K [Bq/kg]	^{60}Co [mBq/kg]
	Earth magnetic field coils	Zhenshi, Jiaxing, China	168 t	IHEP	<0.16	<0.09	<0.4	-
	HDPE	GSE, Thailand	7500 m^2	IHEP	<0.19	0.17±0.05	0.8±0.5	-
	Truss column base, SS	TISCO, Taiyuan, China	2 t	IHEP	<0.16	<0.10	<0.46	-
	Solder	Golden Bridge, Tianjin, China	-	IHEP	<0.14	<0.09	<0.4	-

Table 9. This table presents the radon transparency measurements for the HDPE liner.

Material	Producer	Configuration	Screening	Transparency
5 mm HDPE liner	GSE, Thailand	air / air (3 samples)	CPPM	$(2.6\pm0.4)\times10^{-5}$
		air / water (2 samples)		$(14.2\pm0.9)\times10^{-5}$

Table 10. This table presents the radon emanation measurements. The upper limits are reported at the 90% C.L.

Material	Producer	Quantity measured / Total	Screening	Radon emanation
5 mm HDPE liner	GSE, Thailand	2 m^2 / ~6500 m^2	LP2IB	<1.8 mBq/m^2
20-inch bare PMTs	Huida, Yancheng, China	2 / 15056	LP2IB	<1.9 mBq/PMT
20-inch bare PMT	Hamamatsu, Japan	1 / 4939	LP2IB	<3.4 mBq/PMT
3-inch bare PMTs	Zhanchuang, Hainan, China	29 / 25587	LP2IB	<0.13 mBq/PMT

event recorded in the CD after the muon veto has been applied.

The muon definition and muon-veto strategy are the same as those in Ref. [3]. Muon candidates were identified as CD triggers with charge Q>3×10^4 p.e. or water pool (WP) triggers with Q>700 p.e. We vetoed the full

CPC Accepted

Table 11. Summary of ^{14}C concentration measurements for various LAB samples.

Sample Identifier	^{14}C Concentration [10^{-17} g/g]
Average of 8 times sampling in 2023	2.8 ± 0.2 (stat.) ± 0.6 (sys.)
OSIRIS storage tank (2023.11)	3.4 ± 0.2 (stat.) ± 0.7 (sys.)
JUNO LAB tank (2024.11.20)	3.3 ± 0.4 (stat.) ± 0.7(sys.)

CD for 5 ms following each muon event. This results in a live time efficiency of 95%, which is included in the results presented below.

Apart from potential reconstruction bias, the top and bottom of the JUNO CD are each equipped with an approximately 1-meter-long acrylic chimney section filled with LS. Owing to the thinner water shielding in these regions and the distinctive optical paths of such events, some events originating in the chimneys are reconstructed inside the detector volume (R<17.7 m). To address this issue, dedicated variables for identifying chimney events have been developed in the reconstruction algorithm and can efficiently reject misreconstructed chimney events. A rejection efficiency of 99% is achieved for the region R<17.2 m, while the impact on standard physics events is kept below 1%. A detailed study of chimney event tagging will be presented in the subsequent reconstruction paper. Therefore, the chimney event selection criterion is adopted in the event selection of this study to effectively suppress interference from chimney events.

The event rate distributions in the outer region of the detector for 17.2 m<R<17.5 m and 17.5 m<R<17.7 m are shown in the left and right panels of Figure 4, respectively. The bright spots in the left panel primarily originate from background contributions from acrylic nodes and SS support rods on the outer surface of the acrylic vessel. These components are located closer to the detector, and the gamma rays produced by natural radioactive decay can penetrate deeper. In contrast, the events in the right panel are located closer to the edge and mainly originate from the PMT contribution. Because the PMTs are farther from the LS, with nearly two meters of water shielding, their contribution becomes less significant than that of the acrylic nodes on the outer surface of the acrylic vessel for R<17.5 m.

Figure 5 shows the time evolution of the event rate in the LS for the baseline FV (with R<17.2 m). A gradual decreasing trend is observed, potentially attributable to the combined effects of residual radon decay and purification of the circulating veto water. A small increase in the event rate was observed in early December and late January. The cause remains unknown; possible explanations include water-temperature-induced shifts in the liquid scintillator temperature and the ensuing convection.

A comparison of the event rate in the LS as a function of position between data (from February 5 to March 18, 2026) and the MC simulation [9] is shown in Figure 6. The figure presents the event rate (for events with E>0.7 MeV) for different FV cuts. Each data point represents the total event rate within the volume defined by R<FV, with the dashed line indicating the baseline selection of R<17.2 m. The dominant uncertainty arises from position reconstruction. The uncertainties of the data points are estimated from the variations in event rates caused by position-reconstruction bias, which is derived from the ^{68}Ge calibration source at different z positions. For each data point, we shift its position to the left and right by the corresponding reconstruction bias, compute the event-rate difference between these shifted positions and the original position, and assign this difference as the uncertainty shown in the plot. A detailed numerical comparison between data and simulation is provided in Table 12. The leading systematic uncertainty originates from event reconstruction, whose performance will be further improved in future iterations. The JUNO Collaboration has developed multiple event reconstruction algorithms. Relative to alternative reconstruction implementations, discrepancies in the FV singles rates currently amount to approximately 20–30%. This is mainly due to systematic differences in the reconstructed positions of events occurring near the acrylic vessel. Elsewhere, all algorithms agree closely with one another. The results show that the measured radioactive background from the LS and detector materials within the baseline FV is lower than the

CPC Accepted

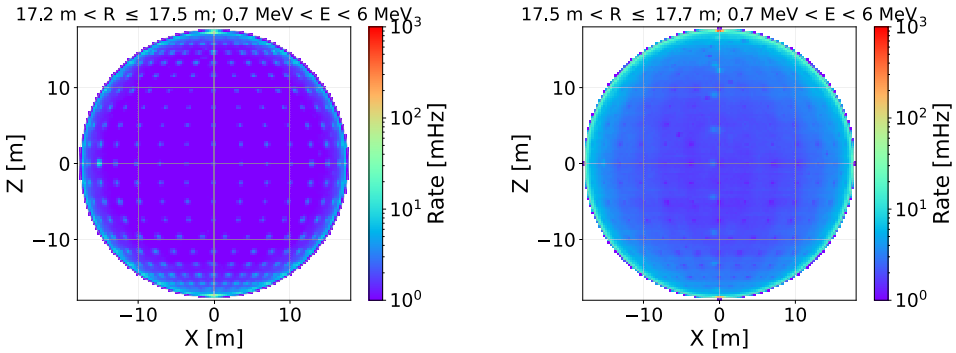

Fig. 4. The x–z distributions of the event rate in the LS over the energy range 0.7–6 MeV are shown for two radial cuts: 17.2 m<R<17.5 m (left) and 17.5 m<R<17.7 m (right).

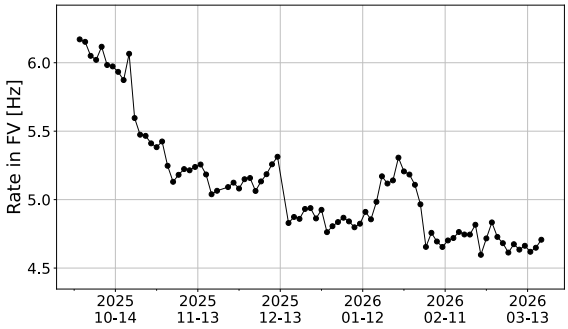

Fig. 5. Time evolution since October 2025 of the rate of events with energies greater than 0.7 MeV in the LS FV within R<17.2 m.

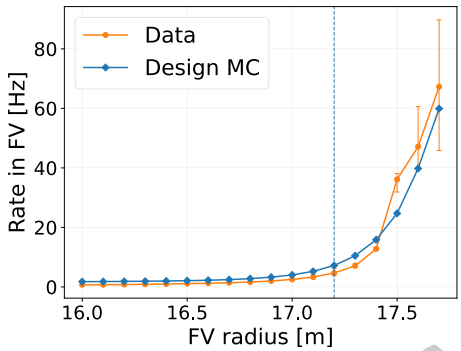

Fig. 6. The figure compares the event rate as a function of the fiducial-volume cut for data collected from February 5 to March 18, 2026 (orange), with the MC simulation from Ref. [9] (blue). The uncertainties on the data points are calculated from the event-rate variations induced by position-reconstruction bias. The dashed line indicates the baseline selection, R<17.2 m.

Table 12. The table compares the event rates above 0.7 MeV within the fiducial volume (R<17.2 m), as obtained from design simulations and experimental data collected from February 5 to March 18, 2026.

	Rate [Hz]	Fiducial volume
Design	LS (10^{-15} g/g U/Th)	2.2
	Other detector material	5
Data	LS + Other detector material	4.7

design value used in the MC simulations. This improvement is consistent with the measured internal radiopurity of the LS, which is approximately one order of magnitude below the design baseline requirement of 10^{-15} g/g for U/Th. As indicated in Table 1, this difference would contribute ∼2 Hz to the LS event rate.

V. SUMMARY

To ensure that the detector achieved sufficiently low background levels, JUNO implemented a rigorous screening campaign to characterize the natural radioactivity of materials during both the R&D and construction phases, involving assays of several thousand samples. This paper presents the quality control results for all materials ultimately deployed in the detector. Using data collected after the completion of LS filling for the JUNO detector, we performed a detailed analysis of the event rate and compared the results with the original MC simulations. The radial distribution of the event rate agrees well with the simulations. The event rate inside the FV meets the design specifications and satisfies the requirements for reactor neutrino oscillation studies.

ACKNOWLEDGEMENTS

We are grateful for the ongoing cooperation of the China General Nuclear Power Group. This work was supported in part by the Chinese Academy of Sciences, the National Key R&D Program of China, the People's Government of Guangdong Province, and the Tsung–Dao Lee Institute of Shanghai Jiao Tong University in China.

We appreciate the contributions of the Institut National de Physique Nucléaire et de Physique des Particules (IN2P3) in France; the Istituto Nazionale di Fisica Nucleare (INFN) in Italy; the Fonds de la Recherche Scientifique (F.R.S.–FNRS) and the Institut Interuniversitaire des Sciences Nucléaires (IISN) in Belgium; the European Structural and Investment Funds, the Czech Ministry of Education, Youth and Sports, and the Charles University Research Center in the Czech Republic; the Deutsche Forschungsgemeinschaft (DFG), the Helmholtz Association, and the Cluster of Excellence PRISMA+ in Germany; the Joint Institute for Nuclear Research (JINR); the Slovak Research and Development Agency in the Slovak Republic; MOST and MOE in Taipei; the Program Management Unit for Human Resources & Institutional Development, Research and Innovation, Chulalongkorn University, and Suranaree University of Technology in Thailand; the Science and Technology Facilities Council (STFC) in the United Kingdom; and the University of California at Irvine and the National Science Foundation (NSF) in the United States.

We also acknowledge the computing resources provided by the Chinese Academy of Sciences, IN2P3, INFN, and JINR, which are essential for data processing and analysis within the JUNO Collaboration.

CPC Accepted

References

[1] Fengpeng An *et al.* (JUNO collaboration), J. Phys. G **43**(3), 030401 (2016)

[2] Angel Abusleme *et al.* (JUNO collaboration), Prog. Part. Nucl. Phys. **123**, 103927 (2022)

[3] Angel Abusleme *et al.*, Nature **654**(8118), 343 (2026)

[4] Angel Abusleme *et al*., Chin. Phys. C **45**(2), 023004 (2021)
[5] Angel Abusleme *et al*., JCAP **10**, 022 (2023)
[6] Jie Zhao *et al*., Astrophys. J. **965**(2), 122 (2024)
[7] Angel Abusleme *et al*. (JUNO collaboration), Chinese Physics C **50**(4), 043001 (2026)
[8] Angel Abusleme *et al*. (JUNO collaboration), JHEP **03**, 004 (2021)
[9] Angel Abusleme *et al*. (JUNO collaboration), JHEP **11**, 102 (2021)
[10] Yuanxia Li *et al*., Radiat. Phys. Chem. **230**, 112579 (2025)
[11] A. Barresi *et al*., The European Physical Journal C **86**(5), 501 (2026)
[12] A. Barresi *et al*. Ultra-trace analysis of 40K in organic liquid scintillators. https://arxiv.org/abs/2607.07376, 2026.
[13] Yuanxia Li *et al*., JINST **18**(05), P05023 (2023)
[14] Chuanya Cao *et al*., Nucl. Instrum. Meth. A **1004**, 165377 (2021)
[15] Giovanni Baccolo *et al*., Eur. Phys. J. Plus **140**(4), 311 (2025)
[16] Xin Ling *et al*., JINST **19**(10), P10004 (2024)
[17] Bin Wang *et al*., JINST **20**(03), P03028 (2025)
[18] Chi Li *et al*., Nucl. Instrum. Meth. A **1063**, 169257 (2024)
[19] Cecilia Landini *et al*., Nucl. Instrum. Meth. A **1069**, 169887 (2024)
[20] Jie Zhao *et al*., Eur. Phys. J. C **86**(3), 236 (2026)
[21] Xuantong Zhang *et al*., Nucl. Instrum. Meth. A **898**, 67 (2018)
[22] Cédric Cerna *et al*., AIP Conference Proceedings **1672**(1), 050002, 08 (2015)

CPC Accepted